The Astrophysical Journal, 882:125 (11pp), 2019 September 10 https://doi.org/10.3847/1538-4357/ab364a

Magnetic Structures at the Boundary of the Closed Corona: A Semi-automated Study of S-Web Morphology

Roger B. Scott[1], David I. Pontin[1], and Peter F. Wyper[2]
[1] School of Science and Engineering, University of Dundee, Dundee DD1 4HN, UK; roger.b.scott@gmail.com
[2] Department of Mathematical Sciences, Durham University, Durham DH1 3LE, UK
Received 2019 June 25; revised 2019 July 26; accepted 2019 July 26; published 2019 September 10

Abstract

Interchange reconnection is thought to play an important role in driving the dynamics of the slow solar wind. To understand the details of this process, it is important to catalog the various magnetic structures that are present at the boundary between open and closed magnetic flux. To this end we have developed a numerical method for partitioning the coronal volume into individual flux domains using volume segmentation along layers of high magnetic squashing degree (Q). Our publicly available implementation of this method is able to identify the different magnetic structures within a coronal magnetic field model that define the open-closed boundary and comprise the so-called Separatrix-Web (S-Web). With this we test previous predictions of how different configurations of high-Q arcs within the S-Web are related to coronal magnetic field structures. Here we present our findings from a survey of 11 different potential field source surface models, spanning from 2008 to 2017, which offer a representative sample of the coronal magnetic field across nearly a complete solar cycle. Two key findings of our analysis are that (i) "vertex" structures—where arcs of the S-Web meet away from the heliospheric current sheet—are associated with underlying magnetic dome structures, and (ii) that any given arc of the S-Web is almost equally as likely to be formed by a narrow corridor of open flux (corresponding to a hyperbolic flux tube) as by the separatrix surface of a magnetic null. Together, these findings highlight the importance of a variety of topological configurations for future studies of interchange reconnection and the acceleration of the solar wind.

Unified Astronomy Thesaurus concepts: Magnetic fields (994); Solar corona (1483); Slow solar wind (1873); Space weather (2037); Solar magnetic reconnection (1504)

1. Introduction

Variations in the velocity, density, and composition of the Sun's "slow" solar wind (SSW) suggest that it is formed by the release of plasma from the magnetically closed corona onto open field lines via interchange reconnection (Crooker et al. 2002; Fisk 2003; Antiochos et al. 2011; Abbo et al. 2016). The viability of this mechanism has been explored in numerical experiments, which have yielded insights into both the latitudinal variation in wind speed (Higginson et al. 2017) and the topological stability of structures at the boundary between closed flux domains and open field regions (Edmondson et al. 2010), where the "fast" solar wind is thought to originate (Habbal et al. 1997). To understand the origins of the SSW we must therefore develop a clear understanding of the structure of the magnetic field at the open-closed boundary (OCB), which encloses the magnetically closed corona. In the simplest dipolar models of the corona, the OCB is composed of the separatrix surface (SS) of the global helmet streamer, whose apex lies along the heliospheric current sheet (HCS); however, it is now clear that in more realistic coronal field models the OCB is also associated with a plethora of SSs and quasi-separatrix layers (QSLs; Antiochos et al. 2011; Platten et al. 2014) that are associated with pseudo-streamers and collectively form the Separatrix-Web (S-Web).

With the recent launch of *Parker Solar Probe* (Fox et al. 2016) and forthcoming launch of Solar Orbiter, in situ data will soon reveal plasma properties in the vicinity of these pseudo-streamers, which are often observed to be associated with SSW outflow (Owens et al. 2013). In order to connect observations to models of the solar corona we require a method for extracting individual structures from within a given magnetic field extrapolation. One way to go about this is to construct the so-called magnetic skeleton, which describes the location of all magnetic nulls, separator lines and SSs (see, e.g., Haynes & Parnell 2010; Platten et al. 2014). The magnetic skeleton is useful for predicting sites of null point and separator reconnection; however, it is of limited use for predicting 3D reconnection in general, as 3D reconnection can also occur in QSLs, away from null points and separators (Galsgaard et al. 2003; Titov et al. 2003; Aulanier et al. 2005; Pontin et al. 2005; Démoulin 2006; Janvier et al. 2013).

A complimentary method involves inspection of the magnetic squashing factor[3] ($Q_\perp$, Titov 2007; Pariat & Démoulin 2012; Tassev & Savcheva 2017; Scott et al. 2018), which is large (or exhibits large gradients) in the vicinity of QSLs, and is formally infinite at genuine topological features. An added benefit to working with $Q_\perp$ is that it is a scalar measure that is preserved along magnetic field lines, so that the gradient of $Q_\perp$ is always perpendicular to the magnetic field. This makes $Q_\perp$ an ideal candidate for volume segmentation, which has been used extensively in medical sciences for the interpretation of 3D tissue scans, which are inherently difficult to visualize.

[3] For this study we use the perpendicular squashing factor, which is less affected by the inclination of the magnetic field at the boundaries of the domain; however, this is not specifically required for what follows.

Table 1
Model Magnetic Fields

Model	Date	GONG Datafile (*.fits)
$\boldsymbol{B}^{(1)}$	2008 Jan 1	`mrbqs080101t0554c2065_258`
$\boldsymbol{B}^{(2)}$	2009 Jan 1	`mrbqs090101t0554c2078_107`
$\boldsymbol{B}^{(3)}$	2010 Jan 1	`mrbqs100101t0554c2092_330`
$\boldsymbol{B}^{(4)}$	2011 Jan 1	`mrbqs110101t0304c2105_194`
$\boldsymbol{B}^{(5)}$	2012 Jan 1	`mrbqs120101t0554c2118_054`
$\boldsymbol{B}^{(6)}$	2013 Jan 1	`mrbqs130101t0424c2132_265`
$\boldsymbol{B}^{(7)}$	2014 Jan 1	`mrbqs140101t0004c2145_129`
$\boldsymbol{B}^{(8)}$	2014 Jul 29	`mrbqs140729t2354c2153_237`
$\boldsymbol{B}^{(9)}$	2015 Jan 1	`mrbqs150101t0004c2159_352`
$\boldsymbol{B}^{(10)}$	2016 Jan 1	`mrbqs160101t0014c2172_214`
$\boldsymbol{B}^{(11)}$	2017 Jan 1	`mrbqs170101t0004c2185_064`

Note. Dates and filenames refer to the GONG magnetogram data used in Potential Field Source Surface magnetic field extrapolations.

In this paper we introduce a new computational technique that can allow us to identify and categorize the different magnetic structures that comprise the S-Web, which will be an essential part of interpreting the wealth of new observations. The method that we describe here is somewhat primitive by comparison to recent advances in medical imaging, which have begun to incorporate neural networks and machine learning (e.g., Liu et al. 2018); however, as the work presented here is a first attempt at applying volume segmentation to coronal magnetic fields, it serves as a proof of concept to be improved in the future. The organization of this paper is as follows. In Section 2 we summarize of our segmentation algorithm and structure classification scheme. In Section 3 we discuss the results of its application to a set of coronal field extrapolations. In Section 4 we discuss the implications of these findings and their relevance to studies of interchange reconnection and the SSW. We then conclude in Section 5 with a few final remarks.

2. Methodology

In this section we provide a brief summary of the various computational tools used in this project. For more details on calculation of the magnetic squashing factor, see Tassev & Savcheva (2017) and Scott et al. (2017). Segmentation and subsequent classification are performed using the `HQVseg` code module, developed by R. Scott using `Python`. A detailed description of the method, which is summarized in Sections 2.3 and 2.4, is available in the documentation. The source code and data cubes containing the magnetic field ($\boldsymbol{B}$) and squashing factor ($Q_\perp$) for each of the 11 models listed in Table 1 can be obtained separately from http://doi.org/10.5281/zenodo.3053415 (Scott 2019).

2.1. Potential Field Source Surface (PFSS) Model Preparation

The model magnetic field is developed in the same manner as described in Scott et al. (2018; hereafter Paper I), beginning with magnetogram data taken from the Global Oscillations Network Group for 11 different samples between 2008 and 2017. To distinguish these models, we shall refer to each with a superscript index following the convention that $\boldsymbol{B}^{(n)}$ is the nth model magnetic field, with the corresponding observation dates given in Table 1.

As in Paper I, the magnetic field is constructed from a PFSS extrapolation, with the source magnetogram data smoothed by a pseudo-Gaussian filter with a characteristic fall-off at angular wave number of $l_f \sim 18$. The dimensions of the model magnetic field are $61 \times 180 \times 360$ in log-radius, sine-latitude, and longitude, respectively, and the domain spans a full spherical shell that extends from the photosphere out to 2.5 solar radii. Additionally, we have calculated the locations of the magnetic nulls within each model using the trilinear method of Haynes & Parnell (2010).

2.2. Squashing Degree

For each model field $\boldsymbol{B}^{(n)}$, we compute the corresponding magnetic squashing factor, $Q_\perp^{(n)}$, using the `qslSquasher` routine (Scott et al. 2017; Tassev & Savcheva 2017). For this project the code has been configured to run on a Linux-based desktop computer hosting an nVidia Tesla k40 GPU. We use trilinear field line tracing with an Eulerian integration step size of 0.25 Mm (equivalent to a minimum of 20 steps per grid cell of the source field).

The output grid is uniformly spaced in angular coordinates and exponentially spaced in the radial coordinate. For most models the grid resolution is $120 \times 480 \times 960$ in radius (r), north latitude (θ), and longitude (ϕ), respectively, and the domain is periodic in ϕ, with $1 \leqslant r/R_\odot \leqslant 2.5$ and $|\theta| \leqslant 88°$. In the case of $\boldsymbol{B}^{(1)}$ the grid resolution of $Q_\perp^{(1)}$ is slightly higher at $150 \times 600 \times 1200$, but the numerical domain is otherwise identical.

Since the squashing factor is a positive definite quantity, whose minimum theoretical value is $\inf(Q_\perp) = 2$, we can adopt the functional representation

$$\mathrm{slog}_{10} Q_\perp = \pm \log_{10} Q_\perp, \tag{1}$$

with the sign taken to be positive or negative where the field lines of the associated mapping are closed or open, respectively. An advantage of this representation is that the collection of SSs that comprise the OCB are bounded on either side by regions of opposite signed $\mathrm{slog}_{10} Q_\perp$, so not only is $Q_\perp$ large (formally infinite) along the OCB, but so too is the gradient of $\mathrm{slog}_{10} Q_\perp$. Note that this convention differs from that of some other authors, who use the sign of $Q_\perp$ to denote the polarity of the magnetic field at the boundary of the domain. A visual representation of $\mathrm{slog}_{10} Q_\perp$ is shown in Figure 1 for the example of $\boldsymbol{B}^{(8)}$, as previously investigated in Paper I.

2.3. Volume Segmentation

Our strategy for partitioning the coronal volume is to use the magnetic squashing factor ($Q_\perp$), which we calculate at every point within the numerical domain (Ω) using the method described above. Regions with large values of $Q_\perp$ or $|\nabla Q_\perp|$, which we call high-Q volumes (HQVs), are indicative of some combination of SSs or QSLs. In either case, these structures serve as boundaries for low-Q volumes that are assumed to correspond to the interior of individual magnetic flux domains. We therefore proceed by attempting to divide the numerical domain into sub-volumes (flux domains) whose boundaries lie within the identified HQVs.

The following is a conceptual description of our segmentation algorithm, which proceeds through the following steps:

1. We first create a mask (M_S) to indicate locations within Ω where the value of $Q_\perp$ (or its gradient) exceeds a

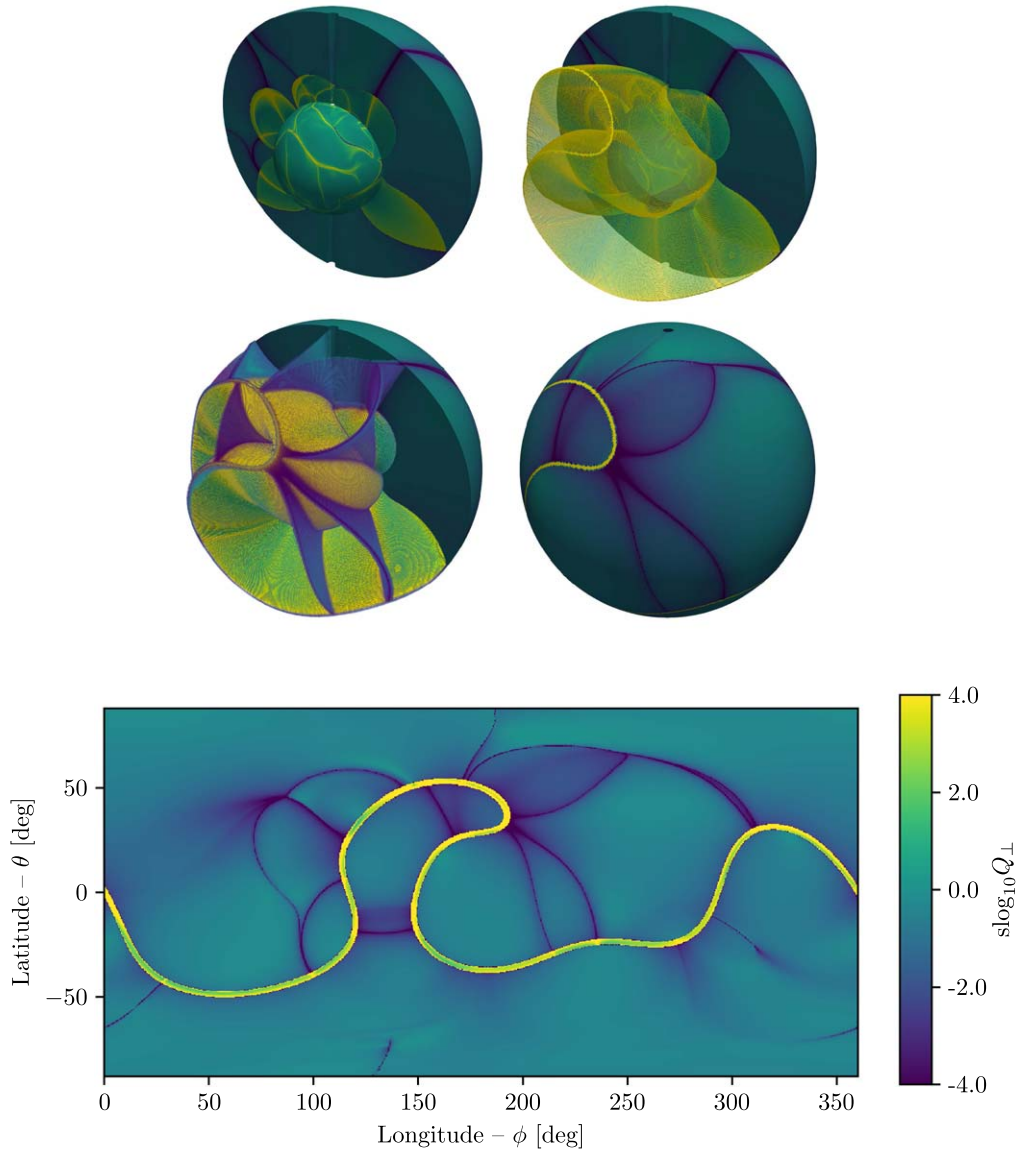

Figure 1. Signed magnetic squashing factor, $\mathrm{slog}_{10}Q_{\perp}$, for model field $\boldsymbol{B}^{(8)}$, is shown in four spherical renderings and one polar slice at constant radius $r \lesssim 2.5\,R_{\odot}$. The top four panels demonstrate the volumetric nature of $\mathrm{slog}_{10}Q_{\perp}$, which is shown at the photospheric level, and in constant longitude slices through the volume (top left). In the top right panel we add in the open-closed boundary as the translucent yellow surface. In the center left panel the high-Q layers that comprise the S-Web are indicated in dark purple. Finally, in the center right panel we overlay the surface rendering of $\mathrm{slog}_{10}Q_{\perp}$ for a constant radius slice at $r \lesssim 2.5\,R_{\odot}$. This same constant radius slice is unwrapped and reproduced in polar coordinates in the bottom panel. The prominent yellow curve indicates closed magnetic flux from just below the apex of the Helmet Streamer, at the base of the heliospheric current sheet.

threshold value. The threshold is determined separately for each PFSS model.

2. Following the initial thresholding, M_S is smoothed and padded to remove "holes" that appear due to numerical artefacts and to ensure that the low-Q regions are compact.
3. Unmasked pixels are assigned region labels, corresponding to individual magnetic flux domains, which we identify through an algorithm that detects compact, simply connected sub-volumes, so that each domain represents a flux tube with a low-Q interior surrounded by a high-Q flux surface.
4. In the case of a global field model, labeling is reconciled across the $\phi = 0$ boundary to enforce periodicity in the label map.
5. Points within M_S are then subsumed by adjacent flux domains using a "watershed" approach, which takes the pre-existing domain labels as seeds and then grows each volume into the unlabeled region while attempting to place region interfaces at "ridges" in $Q_{\perp}$.

This completes the partitioning of Ω into distinct magnetic domains, Ω_i, as shown by the different colored regions in Figure 2 for the $\boldsymbol{B}^{(8)}$ example. For a more detailed description of the segmentation algorithm see the `HQVseg` documentation. Having identified the individual sub-volumes in this way, it remains to identify the various portions of the HQV (shown in black) that are responsible for this partitioning, thus allowing us to identify the individual structures that comprise the S-Web.

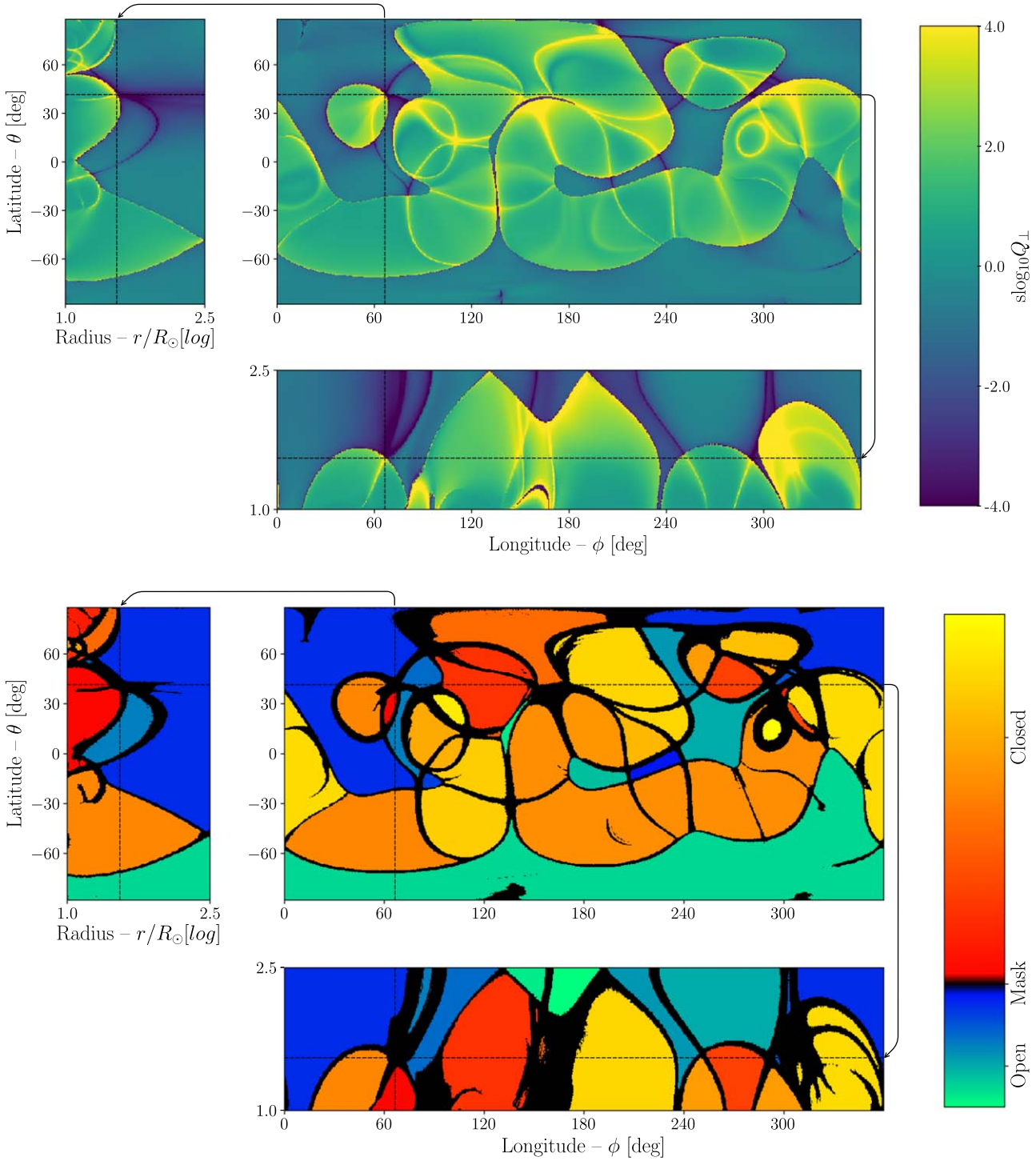

Figure 2. Top: a three-panel view of the magnetic squashing factor ($\mathrm{slog}_{10}Q_\perp$) for model field $\boldsymbol{B}^{(8)}$, with slices of constant radius, latitude, and longitude, corresponding to the location of an important coronal null (N_2, as discussed in Paper I). Cross-hairs indicate where the panels intersect. Bottom: identical panel view showing High-Q mask (M_S) and segmented domains, Ω_i.

2.4. HQV Classification

In the following, we summarize the procedure for cataloging different subelements of the collective HQV. We refer to the set of all points within the collective HQV as S, while S_i refers to subsets of S that lie within a threshold distance of a given domain, Ω_i. Points within S that associate with at least two domains are referred to as "interface HQVs," while those that are contained entirely within a single domain are referred to as "non-interface HQVs," and we treat these cases separately.

For a given pair of flux domains, Ω_i and Ω_j, we define the interface HQV, S_{ij}, as the intersection of S_i and S_j. HQVs of this type comprise the bulk of S, and account for the majority of "simple" and "branching" arc segments, as discussed in Paper I. In short, a simple HQV meets the main helmet streamer at both of its ends in any radial cut while a branching segment meets with other arcs away from the helmet streamer

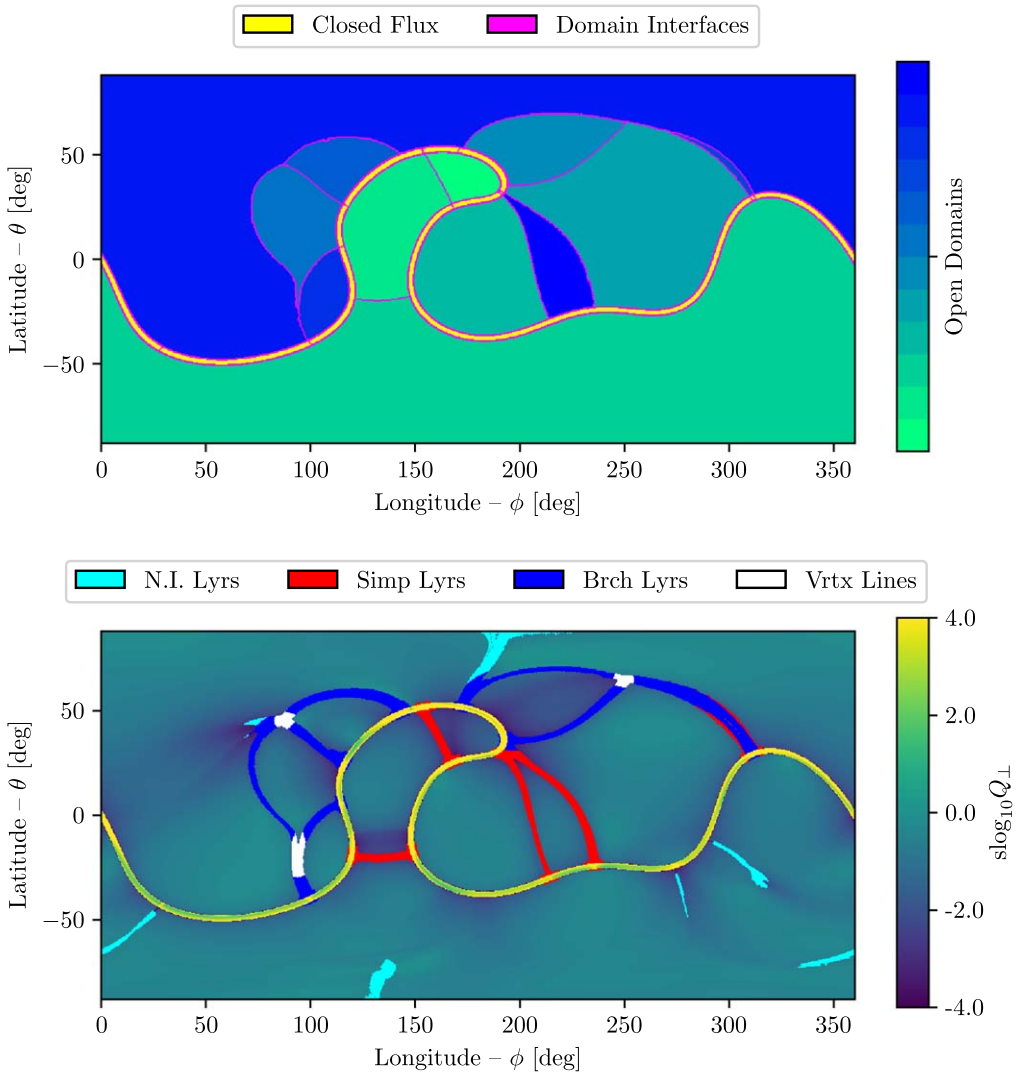

Figure 3. Example of high-Q structure identification for model field $\boldsymbol{B}^{(8)}$. Various open flux domains are indicated in the top panel, with domain boundaries shown in magenta and closed flux from within the global helmet streamer indicated in yellow. In the bottom panel, subelements of the collective high-Q volume (S) are colored by their type (red for simple layers, blue for branching layers, cyan for non-interface layers, and white for vertex lines), as identified by the classification algorithm.

(see below for further details, and Figure 3 for some examples). From the collection of interface HQVs we can then find the HQV associated with the intersection of any arbitrary set of more than two domains, $S_{i\ldots pq}$, from the intersection of their parent entries, $S_{i\ldots p}$ and $S_{i\ldots q}$, and these account for the majority of "vertices" (intersections of branching arc segments) as discussed in Paper I (see Figure 3).

For HQVs that occur away from domain boundaries, we first find the subsets of S that are entirely within individual domains Ω_i and not already a part of the collection of interface HQVs, and these we call $\tilde{S}_i$. Since any given region can support multiple non-interface HQVs, each $\tilde{S}_i$ is then divided into constituent elements $\tilde{S}_i^k$, which are identified and labeled using a simplified version of the segmentation procedure described above. As well as accounting for the "detached" arcs described in Paper I—i.e., HQV structures that form only a single connection to the HCS in any radial slice—non-interface HQVs ($\tilde{S}_i^k$) form a compliment to interface HQVs (S_{ij}) so that, apart from a few small regions that do not survive the thresholding, these two groups approximately span the collective HQV (S).

Once all of the individual HQV structures have been identified, their proximities to each other and to the various coronal magnetic nulls are recorded. This allows for sorting of individual structures into classes, whose members share certain common properties. In Paper I we chose a categorical scheme for describing features in the S-Web in terms of their intersections with each other and with the HCS. We now revisit those definitions in the context of our newly identified HQV structures.

Recall that a "high-Q arc" (HQA) is a quasi-linear feature in constant-radius slice through the S-Web in the extended corona (for our purposes, on the outer boundary, at $2.5R_\odot$). The extension of an HQA into 3D is a sheet-like structure that we refer to as a "high-Q layer" (HQL), which may be associated with either (or both of) an SS or a QSL, as in the example of Titov et al. (2011). In the following, we consider only HQLs that are associated with open flux domains and we restrict our attention to those that do not span or form a significant portion of the global helmet streamer, i.e., high-Q structures that are embedded predominantly in a single polarity of open flux. We classify these as follows:

1. By analogy to *vertices*, we identify a *vertex line* as the intersection of three or more HQLs, which forms a pseudo-line element that intersects the outermost boundary at a point away from the HCS.
2. By analogy to *branching segments* we identify a *branching layer* as any HQL that is bounded by at least one vertex line.
3. By analogy to *simple segments* we identify a *simple layer* as any HQL that coincides with a domain boundary and connects to the HCS but does not intersect a vertex line.
4. And where we previously use *detached segments* to refer to structures that exhibited one or fewer intersections, we shall instead use the term *non-interface layer* to describe any HQL that is contained entirely within a single flux domain, noting that the logical extension of a *detached segment* is a subset of this class.

In practice this classification scheme relies on a complex set of rules for determining the morphology and connectivity of individual structures, and these are detailed in the `HQVseg` documentation. An example implementation of this classification scheme is given in Figure 3 for model field $\boldsymbol{B}^{(8)}$, which shows a 2D cut near the outer radial boundary, where the imprints of a representative set of these structures (as identified by the algorithm) are displayed. Note that while each of the indicated HQV elements is a fully 3D structure, within this 2D cut their properties are consistent with the 2D class types described in Paper I.

3. Results

In each of the preceding figures we have used the familiar example of $\boldsymbol{B}^{(8)}$ from 2014 July 29. The 10 remaining models are depicted in Figure 4, which shows the shape of the HCS and myriad HQAs in each case. After applying our method to all 11 models, we then tabulated the total number of identified structures within each model and over the aggregate. The results are listed in Table 2, and summarized in Figure 5, and from these we can begin to address some of the questions regarding both the viability of our method and the properties of HQLs.

3.1. How Robust is the Algorithm?

The method that we have developed for identifying structures within the magnetic field is heavily reliant on our ability to accurately resolve the shape of individual magnetic flux domains. This can be problematic for HQLs that extend into the low corona, where closed flux domains make up an increasingly large proportion of the total flux, and open domains are squeezed to progressively narrower regions, whose width may be less than the grid size of the numerical representation. In order to characterize this limitation, we have estimated the number of simple layers that do not (a) have a photospheric footprint, or (b) contain a magnetic null, of which the total should be zero if the method were to perform perfectly. In practice, the performance is less than perfect, with only $43/57$ ($\approx$75%) satisfying one condition or the other.

Since branching layers are expected to form by the same fundamental mechanism as simple layers—namely, either a narrow corridor HFT or an SS from a corridor of zero width—we expect that the same benchmark should apply. Because branching layers are defined by their association with vertices, which are expected to be strongly correlated with coronal magnetic nulls, we count the instances in which a branching layer is associated with at least one null that does not lie within a vertex line. When combining this result with the number of branching layers that have a photospheric footprint, we find that $49/67$ ($\approx$73%) satisfy one condition or the other. Taken together, these estimates suggest that our method is able to fully resolve roughly 75% of HQLs to their lowest extent in the coronal volume.

An additional difficulty arises from the fact that merging HQLs, which can remain very close together at distances relatively far from the HCS, lead to the occasional false detection of vertex lines. We observe that the most common cause of this misidentification is a large, dome-like herniation of the OCB, which is morphologically similar to a null separatrix dome, but which lacks the characteristic null at its apex. This occurs in cases where there is a strong horizontal field component that either (1) causes the null to be subsumed by the flux beneath the helmet streamer, which is itself "draped" over the top of the dome, or (2) causes the null to be positioned below the photosphere, so that the dome itself is, in fact, a bald-patch SS.

In either of these cases, the HQLs associated with these structures appear, at low resolution, to intersect at a vertex line, but upon closer inspection it can be seen that they do not intersect, but run parallel over large distances before diverging abruptly. These cases can be distinguished by close inspection of the angle between the two boundaries of the smallest domain within the detected vertex line, which goes to zero for merging layers but remains finite at a genuine vertex line. In order to address this point of weakness, we have included a crude estimate of this merging angle, which we find by comparing the contribution from each flux domain to the total volume within a given vertex line, and this appears to be an effective, albeit imperfect, means of differentiating between the two cases.

3.2. Are Vertex Lines Indicative of Open Spine Lines?

From the results listed in Table 2, we see that of the 22 vertex lines identified, only 14 ($\approx$64%) associate with a coronal null. If, however, we subtract the number whose merging angle is highly acute ($8/22$), the agreement is very good over the aggregate; although outliers remain within individual models. Given these limitations, which are likely to be persistent at some level for any automated detection scheme, it seems appropriate to revisit our prediction from Paper I regarding the association of null spine lines with intersections of HQAs in the outermost imprint of the S-Web. In particular, it now seems that where a vertex can be robustly distinguished from a group of merging layers, the association with a spine line from a magnetic null is very good; however, and perhaps more importantly, it appears that even for crude vertex detections, which are insensitive to the merging angle within the vertex, the association with magnetic dome structures underlying open flux domains is highly robust, with the distinction being that roughly one-third of such domes do not appear to support a magnetic null.

3.3. Are High-Q Layers Indicative of Separatrix Surfaces?

There are two proposed formation mechanisms for HQLs in the S-Web, these being narrow corridors of open flux, and SSs from coronal null points (Antiochos et al. 2011; Titov et al. 2011). The distinction between these will likely be important to

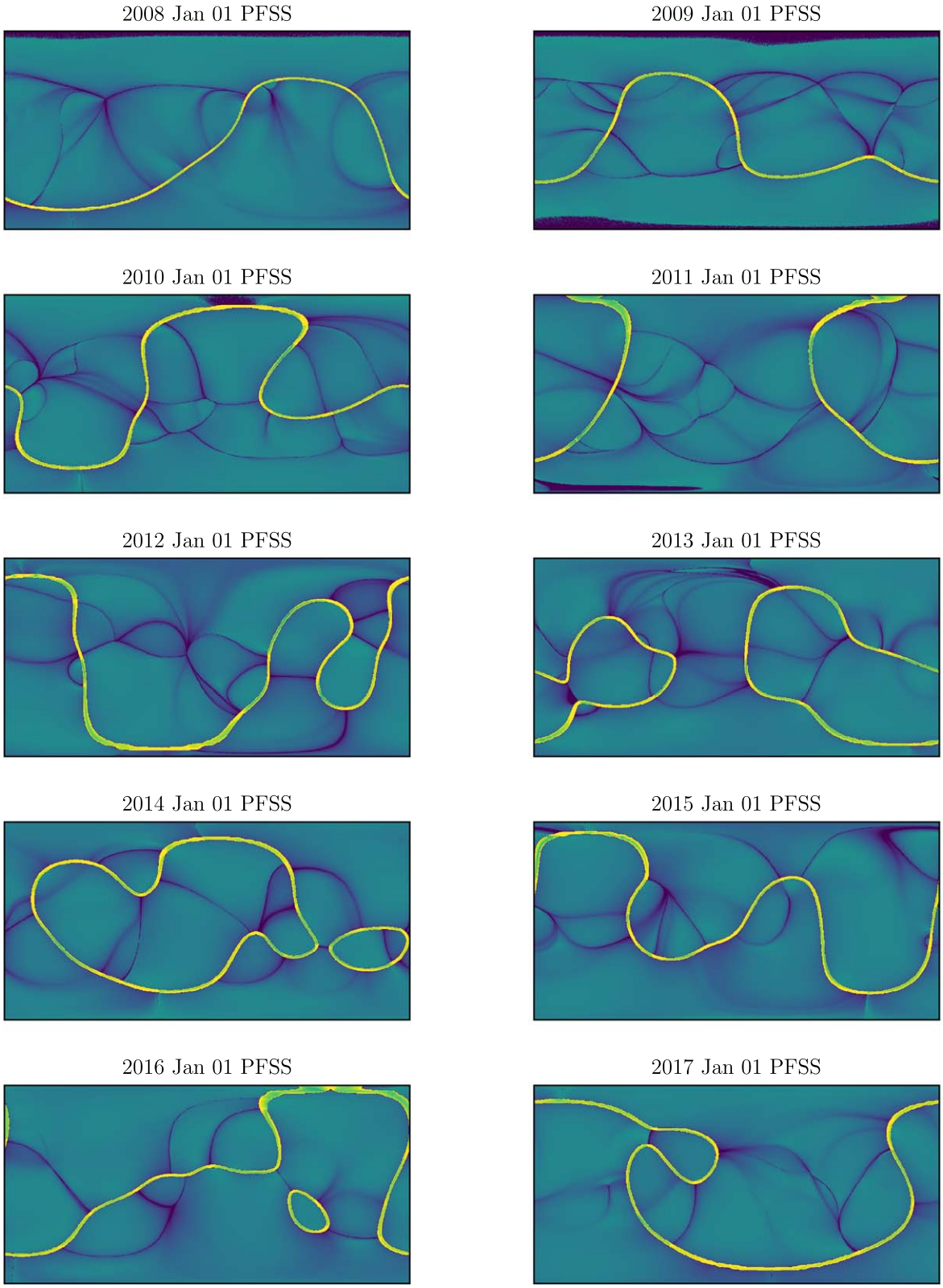

Figure 4. Representative maps of the S-Web for a set of Potential Field Source Surface (PFSS) extrapolations from GONG magnetogram data captured on January 1, every year from 2008 to 2017. In each panel the value of $\mathrm{slog}_{10}Q_{\perp}$ is shown in a 2D cut just below $2.5R_{\odot}$, using the same color scale and coordinates as in the lower panel of Figure 1.

the dynamics of interchange reconnection and the deposition of plasma from the closed corona onto open field lines. From inspection of $Q_{\perp}$ at the source surface alone, it is impossible to differentiate between these structures; however, we can distinguish them by testing for the presence of a magnetic null within a given HQL. This test does not guarantee that the HQL contains an SS, as the null point could be associated with a low-lying magnetic dome within a larger corridor (see

Table 2
Summary of Results

Model	$\boldsymbol{B}^{(1)}$	$\boldsymbol{B}^{(2)}$	$\boldsymbol{B}^{(3)}$	$\boldsymbol{B}^{(4)}$	$\boldsymbol{B}^{(5)}$	$\boldsymbol{B}^{(6)}$	$\boldsymbol{B}^{(7)}$	$\boldsymbol{B}^{(8)}$	$\boldsymbol{B}^{(9)}$	$\boldsymbol{B}^{(10)}$	$\boldsymbol{B}^{(11)}$	Aggregate
Vertex Lines												
Total	1	6	4	3	2	1	0	3	1	1	0	22
Conn. OCB	1	5	3	3	1	0	0	3	1	1	0	18
Conn. Phot.	0	0	0	1	0	0	0	0	0	0	0	1
Assoc. Null	0	5	4	0	2	0	0	2	0	1	0	14
Acute	1	1	1	1	1	1	0	1	1	0	0	8
Branching Layers												
Total	3	20	10	10	8	2	0	8	3	3	0	67
Conn. OCB	3	20	10	10	8	2	0	8	3	3	0	67
Conn. Phot.	0	7	2	5	2	1	0	1	1	0	0	19
Assoc. Null	3	16	10	3	8	1	0	7	2	3	0	53
Assoc. Null (non-vertex)	3	8	7	3	2	1	0	2	2	2	0	30
Simple Layers												
Total	0	3	7	0	10	8	13	6	3	4	3	57
Conn. OCB	0	3	7	0	10	8	13	6	3	4	3	57
Conn. Phot.	0	1	2	0	3	2	5	3	2	1	1	20
Assoc. Null	0	1	5	0	4	3	2	2	1	3	2	23
Non-interface Layers												
Total	8	4	5	9	1	7	2	4	5	2	7	54
Conn. OCB	6	4	5	9	1	7	2	4	5	2	7	52
Conn. Phot.	3	3	1	3	0	2	0	1	2	1	2	18
Assoc. Null	1	3	1	3	0	2	0	3	0	0	3	16
All Layers												
Total	12	33	26	22	21	18	15	21	12	10	10	200
Conn. OCB	10	32	25	22	20	17	15	21	12	10	10	194
Conn. Phot.	3	11	5	9	5	5	5	5	5	2	3	58
Assoc. Null	4	17	17	6	8	6	2	9	3	6	5	83
Magnetic Nulls												
Total	20	32	29	19	16	23	10	14	12	16	10	201
OCB	12	22	20	10	8	10	2	10	4	9	7	114
Closed	8	10	9	9	8	13	8	4	8	7	3	87
Assoc. Vtx. Line	0	5	3	0	2	0	0	2	0	1	0	13
Assoc. Brch. Lyr.	5	14	10	8	4	1	0	4	2	3	0	51
Assoc. Smp. Lyr.	0	2	7	0	4	3	2	2	2	4	2	28
Assoc. N.I. Lyr.	1	5	1	4	0	3	0	4	0	0	5	23

Note. The number of occurrences of each type of structure (simple and branching layers, vertex lines, and non-interface layers) are listed for each model and summed in aggregate. Additionally, for each model we list the number of magnetic nulls and their associations with structures of each type.

discussion in Paper I). Nonetheless, it can be used to differentiate open corridors that lack any internal topological structures from more complex configurations.

If we consider only simple layers (excluding those that have neither a magnetic null nor a photospheric footprint, as per the above discussion), we find that the distribution between these is approximately even. For branching layers (again, disregarding magnetic nulls associated with vertex lines), we find that the distribution is closer to 2:1 (see Table 2). This suggests that SSs may be present in a large portion of all HQLs, possibly even a majority. Additionally, while the mechanisms responsible for their formation are probably the same, branching layers may be more likely to contain SSs when compared to simple layers.

3.4. Are Non-interface Layers Fundamentally Different?

Considering non-interface layers, we first note that a significant number of detected cases terminate at one of the poles, and these are assumed to be artefacts of the magnetic field interpolation in that region. For non-polar cases, we anticipate two main formation mechanisms, the first being the familiar case of a detached layer, in which an HQV is formed at a narrow (possibly singular) corridor, which is bounded by at least one isolated magnetic dome. The important feature that distinguishes this configuration from a group of branching layers is the isolation of the separatrix dome, which can support no other HQV structures, this being critical to the fact that the non-interface layer does not partition any flux domains. The second formation mechanism, which was not discussed in Paper I, results from an HFT having a relatively weak signature

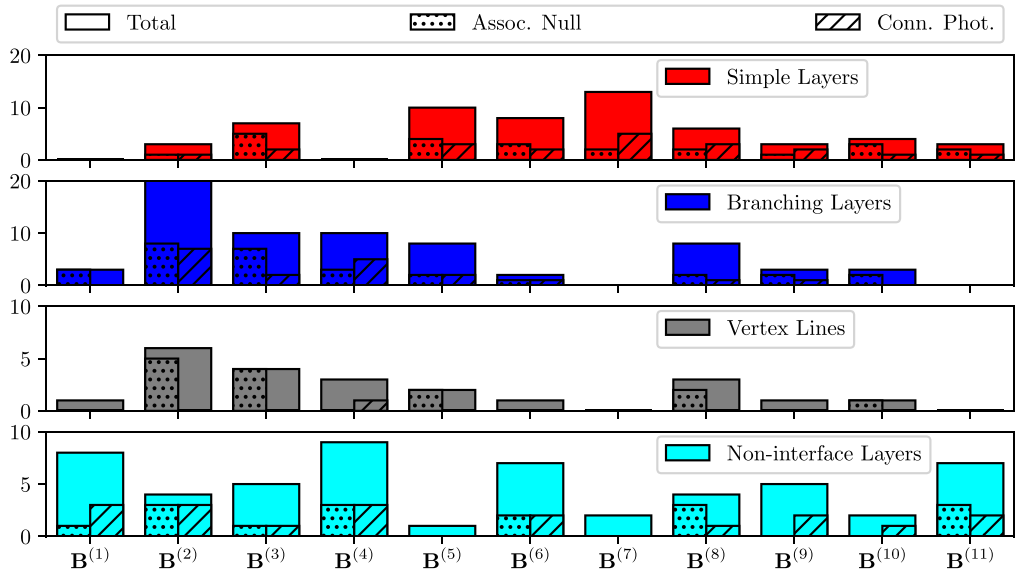

Figure 5. Number of detected high-Q structures within each model magnetic field. The four panels show the results for simple layers (red), branching layers (blue), vertex lines (gray), and non-interface layers (cyan). Within each panel, the solid color indicates the total number, while dotted and hashed indicate the number that associate with a magnetic null (non-vertex in the case of branching layers) and the number that have a photospheric footprint, respectively.

in $Q_\perp$ (or $|\nabla Q_\perp|$), which appears to "fade out" in the middle and is divided into multiple, disconnected pieces.

In the first case, we expect that such structures should exhibit a superposition of the traits associated with vertex lines and branching layers, while in the latter case they are expected to be more like simple layers that form above "not-so-narrow" open corridors, probably in the absence of any magnetic nulls. These assertions are roughly supported by our findings in Table 2, in which we see that there is, again, a roughly even split (16:18) between non-interface layers that support a null and those that have a photospheric connection, with the number of identified cases that have either one or the other (or both) being 34 out of a total of 54 (≈63%)—lower than the value for simple or branching layers. Notably, the fraction of all non-interface layers that support a magnetic null, being 16/54 (≈30%), is significantly lower than the value for vertex lines, indicating that the majority of these most likely do not support a magnetic null and associated spine line, as would be expected in the case of a detached layer.

3.5. Where are Magnetic Nulls Preferentially Found?

If we consider the occurrence of magnetic nulls across all 11 models, we find that just under half of those detected are exclusive to the closed field (87/201 or ≈43%), while the bulk are associated with open field structures that connect to the OCB (simple or branching layers, vertex lines, and non-interface HQLs), and in many cases these nulls associate with multiple such structures (e.g., nulls that associate with vertex lines also associate with the corresponding branching layers, as described above). Notably, over the entire data set, every null can be associated with at least one closed field domain, so that all nulls are either entirely in the closed field region or are a part of the OCB, with none being isolated within or between open flux domains. Thus, the likelihood of finding an HQL that supports a magnetic null and does not connect to a closed-field domain somewhere in the coronal volume appears to be extremely low. This finding is supported by the fact that, of all the interface and non-interface HQVs identified, only 6/200 (3%) do not have a connection to the OCB somewhere within the domain.

Additionally, for each type of high-Q structure, we have estimated the typical radius at which the associated magnetic nulls are found. For vertex lines we find a mean value of 1.65 $R_\odot$, while for branching layers the average height (again, disregarding vertex-associated nulls) is somewhat less (1.25 $R_\odot$). Simple layers have the lowest typical null formation height, at 1.21 $R_\odot$, and non-interface layers again behave as an intermediate case, with nulls being typically found at 1.27 $R_\odot$.

On close inspection of the distribution of nulls, we find that 13 of these associate with vertex lines, compared to the 14 vertex lines that support a magnetic null, indicating a possible double counting of a vertex line in model $\boldsymbol{B}^{(3)}$. Regarding nulls that associate with branching, simple, and non-interface layers, we find that in every case there are more of these than there are layers of each kind that identify with a null, indicating the prevalence of corridor structures that support not one magnetic null, but several. This seems to be especially true of branching layers, for which the number of identified non-vertex nulls is nearly double the number of layers that identify with a non-vertex null.

3.6. Is there a Dependence on Solar Cycle?

Since our models are (nearly) evenly spaced over an entire solar cycle, one could ask whether the structure of the S-Web within a given model depends on solar activity. It would be reasonable to expect that the presence of large bipolar regions might increase the complexity of the OCB, and, indeed, it has been shown (see, e.g., Riley et al. 2002) that the latitudinal extent of the HCS generally increases during solar maximum. We might expect, therefore, that the total number of HQAs would be larger for models with larger magnetic flux concentrations at mid-latitude.

In fact, what we find is that there appear to be generally more simple layers and fewer branching layers and vertex lines near solar maximum, but that the total number of HQLs does not exhibit any obvious trend. This may be related to the tendency

for simple layers to form along the "concave" side of the HCS, in regions where there is a large excursion of open flux into the hemisphere of the predominantly opposite polarity; however given the sparsity of our samples we are not prepared to draw definitive conclusions on this point.

4. Discussion

In Section 3 we presented our findings from the ensemble of 11 different PFSS models, spanning nearly a solar cycle. The size of our sample set is constrained by the computational intensity of the 3D calculation of $Q_\perp$ and subsequent volume segmentation, and while we have attempted to include as many individual models as is feasible, the total number of structures identified within each model and over the aggregate are too few to allow for robust statistics. Nonetheless, our results offer a representative sample of the variety of HQLs that comprise the S-Web, and are indicative of the kinds of structures that are present in (static models of) the solar corona.

Regarding detached layers and simple layers, we find that the key difference, being the association with a vertex line, informs the context regarding the surrounding field (i.e., the presence of an adjacent dome-like structure), but that the details of the magnetic field within the structures themselves are likely to be nearly identical. In both cases, as the HQL is traced downward it becomes progressively narrower until it either (1) terminates at a coronal null, or (2) eventually intersects the solar surface along a very narrow corridor of open flux. In either case, magnetic flux that permeates the HQL is composed of field lines that pass very close to the OCB, and is therefore likely to be an excellent indicator for locations where reconnection could preferentially deposit closed coronal material into the open field. And since reconnection processes that occur in these structures are likely to be affected by the presence of a magnetic null, this inability to differentiate such topological features based on the morphology of the S-Web makes it all the more important to understand the reconnection dynamics associated with the various possible subtypes.

Considering vertex lines and their association with magnetic dome structures, we find that where these can be robustly distinguished from the merging of nearby HQLs, the association is very good; however, the current method employed for this distinction is cumbersome, making the utility of these detections somewhat limited. This difficulty is likely to be a persistent feature of any method that uses volume segmentation unless the resolution of the rendering is extremely high, or there is a significant improvement in the sophistication of the feature detection methods. It is noteworthy that even in cases where the method fails, the morphology of the OCB in the underlying field is all but indistinguishable from a null dome configuration, save that the null (or bald patch) is positioned at a point along the surface of the dome that makes it difficult to associate with the merging point (vertex line) of the various open field domains. Thus, while the detection of vertex lines may prove to be an imperfect indicator of magnetic nulls, it remains an excellent indicator for dome-like structures along the OCB. All of the above shows that it is possible to infer some, but not all, aspects of the topology and morphology of coronal magnetic fields from inspection of HQLs in the S-Web, and this in turn informs our understanding of the types of structures that should be considered for dynamical studies of the sources of the SSW.

Importantly, the conclusions drawn herein are based on potential magnetic field extrapolations, from magnetogram data that are quite heavily smoothed. It is well known that the topological structures in the corona are dependent on both the resolution and the field model (Longcope & Parnell 2008; Platten et al. 2014; Edwards et al. 2015), and it will therefore be important to explore these aspects in future. Additionally, the (near total) absence of HQV structures that do not connect to the OCB is likely a feature of static models, which do not capture the influence of dynamic structures such as coronal mass ejections. It is worth noting, however, that the presence of magnetic nulls at large-to-moderate heights is typically found to be robust to these factors (increases in resolution generally lead to an increase in the number of nulls close to the photosphere), and these null points at large heights will be associated with larger closed flux domains. Thus, reconnection at those nulls and associated separators should presumably provide the largest contributions in the release of plasma from the closed field to the open field.

5. Conclusions and Outlook

We have presented here a novel method for analyzing coronal magnetic field models, which will be described in greater detail in a forthcoming publication, as well as an implementation of the method, which we have made publicly available (Scott 2019). We have also generated a representative set of 11 PFSS extrapolations, which are available along with our implementation, and we encourage members of the community to download and inspect these for themselves. After applying the method to our data set, we performed a survey of the number of occurrences of various structures within each model, as well as over the aggregate. Our main conclusions are as follows:

1. Segmentation of the coronal volume is a powerful and promising method for identifying individual structures in the solar corona and cataloging their rates of occurrence. We have described here one approach to doing this, but there are likely to be other, more sophisticated methods (especially involving machine learning and neural networks), that can and should be explored in the future.
2. Any given layer of the S-Web appears to be approximately equally likely to contain a null (likely implying the presence of a separatrix curtain) or not (implying the presence of a narrow corridor of open flux constituting a QSL/HFT), and both configurations should be considered as potential sites of interchange reconnection.
3. Vertex lines, where multiple HQLs join, are often indicative of spine lines from coronal null dome structures, but these can also be associated with dome structures that exhibit no open spine line, either because the dome is subsumed by the GHS, or because the dome is itself a bald-patch SS.

As per the discussion in Scott et al. (2018), it is reasonable to expect there might be substantial differences between the observational signatures of interchange reconnection in narrow corridors and in singular corridors (containing magnetic nulls). This conjecture is based on the supposition that different lengths of closed magnetic field lines might typically be taking part—in the presence of embedded null domes the field lines should typically be shorter and lower-lying—and the properties of the plasma along such field lines could differ significantly. In

particular, we anticipate that the rate of reconnection, as well as the temperature, abundance ratios, and charge state of the plasma near the reconnection site, could differ dramatically between the various cases we have described, all of which carry significant implications for in situ observations of the inner heliosphere, such as those expected from the recently launched *Parker Solar Probe*. We therefore advocate for numerical experiments that explore how interchange reconnection may be affected by the presence of one or more magnetic nulls within the narrow corridors commonly associated with the S-Web, with the aim to incorporate progressively more complex magnetic configurations, so that the contribution of each type of structure within the ensemble of the S-Web can be better understood in the context of the dynamics of the SSW.

This work uses data obtained by the Global Oscillation Network Group program, managed by the National Solar Observatory, which is operated by AURA, Inc. under a cooperative agreement with the National Science Foundation. The data were acquired by instruments operated by the Big Bear Solar Observatory, High Altitude Observatory, Learmonth Solar Observatory, Udaipur Solar Observatory, Instituto de Astrofsica de Canarias, and Cerro Tololo Interamerican Observatory. This work is supported by the UK's STFC under grant ST/N000714/1. P.F.W. is supported through the award of a Royal Astronomical Society Fellowship. We thank our colleagues, S.K. Antiochos, C.R. DeVore, and A.K. Higginson, for helpful insights and discussion. We also thank the anonymous referee for their careful attention to the manuscript.

ORCID iDs

Roger B. Scott https://orcid.org/0000-0001-8517-4920
David I. Pontin https://orcid.org/0000-0002-1089-9270
Peter F. Wyper https://orcid.org/0000-0002-6442-7818

References

Abbo, L., Ofman, L., Antiochos, S. K., et al. 2016, SSRv, 201, 55
Antiochos, S. K., Mikić, Z., Titov, V. S., Lionello, R., & Linker, J. A. 2011, ApJ, 731, 112
Aulanier, G., Pariat, E., & Démoulin, P. 2005, A&A, 444, 961
Crooker, N. U., Gosling, J. T., & Kahler, S. W. 2002, JGR, 107, 1028
Démoulin, P. 2006, AdSpR, 37, 1269
Edmondson, J. K., Antiochos, S. K., DeVore, C. R., Lynch, B. J., & Zurbuchen, T. H. 2010, ApJ, 714, 517
Edwards, S. J., Yeates, A. R., Bocquet, F. X., & Mackay, D. H. 2015, SoPh, 290, 2791
Fisk, L. A. 2003, JGRA, 108, 1157
Fox, N. J., Velli, M. C., Bale, S. D., et al. 2016, SSRv, 204, 7
Galsgaard, K., Titov, V. S., & Neukirch, T. 2003, ApJ, 595, 506
Habbal, S. R., Woo, R., Fineschi, S., et al. 1997, ApJL, 489, L103
Haynes, A. L., & Parnell, C. E. 2010, PhPl, 17, 092903
Higginson, A. K., Antiochos, S. K., DeVore, C. R., Wyper, P. F., & Zurbuchen, T. H. 2017, ApJL, 840, L10
Janvier, M., Aulanier, G., Pariat, E., & Démoulin, P. 2013, A&A, 555, A77
Liu, F., Zhou, Z., & Samsonov, A. 2018, Magn. Reson. Med., 79, 2379
Longcope, D. W., & Parnell, C. E. 2008, SoPh, 254, 51
Owens, M. J., Crooker, N. U., & Lockwood, M. 2013, JGRA, 118, 1868
Pariat, E., & Démoulin, P. 2012, A&A, 541, A78
Platten, S. J., Parnell, C. E., Haynes, A. L., Priest, E. R., & Mackay, D. H. 2014, A&A, 565, A44
Pontin, D. I., Galsgaard, K., Hornig, G., & Priest, E. R. 2005, PhPl, 12, 052307
Riley, P., Linker, J. A., & Mikić, Z. 2002, JGRA, 107, 1136
Scott, R. B. 2019, HQVseg—A Python Module for Coronal Volume Segmentation, Ver. 1.0, Zenodo, doi:10.5281/zenodo.3053415
Scott, R. B., Pontin, D. I., & Hornig, G. 2017, ApJ, 848, 117
Scott, R. B., Pontin, D. I., Yeates, A. R., Wyper, P. F., & Higginson, A. K. 2018, ApJ, 869, 60
Tassev, S., & Savcheva, A. 2017, ApJ, 840, 89
Titov, V. S. 2007, ApJ, 660, 863
Titov, V. S., Galsgaard, K., & Neukirch, T. 2003, ApJ, 582, 1172
Titov, V. S., Mikić, Z., Linker, J. A., Lionello, R., & Antiochos, S. K. 2011, ApJ, 731, 111